

HIGH ENERGY DENSITY RESEARCH CENTER
Russian Academy of Sciences
IVTAN, Izhorskaya 13/19, Moscow, 127412 Russia
Telex 411959 IVTAN SU, Telephone (095) 485-79-88, Fax: (095) 485-79-90

**EDGE EFFECTS AT SPALL FRACTURE
FOR TITANIUM ALLOYS OF VARYING OXYGEN CONTENT**

Final Technical Report
by
G.I.Kanel, S.V.Razorenov, A.V.Utkin
(September, 18, 1997 - July 1, 1998)

United States Army
EUROPEAN RESEARCH OFFICE OF THE U.S.ARMY
London, England

CONTRACT NUMBER: N68171-97-M-5772

Contractor: **S.V. Razorenov**

Approved for Public Release; distribution unlimited

1998

DTIC QUALITY INSPECTED 2

19990202 042

REPORT DOCUMENTATION PAGE			Form Approved OMB No. 0704-0188	
1. AGENCY USE ONLY (Leave Blank)		2. REPORT DATE 1 September 98	3. REPORT TYPE AND DATES COVERED Final Report (18 Sep. 97 – 1 July 98)	
4. TITLE AND SUBTITLE EDGE EFFECTS AT SPALL FRACTURE FOR TITANIUM ALLOYS OF VARYING OXYGEN CONTENT			5. FUNDING NUMBERS C - N68171-97-M-5772	
6. AUTHOR(S) Sergey V. Razorenov, Gennadii I. Kanel, Alexander V. Utkin				
7. PERFORMING ORGANIZATION NAME(S) AND ADDRESS(ES) HIGH ENERGY DENSITY RESEARCH CENTER of Russian Academy of Sciences, IVTAN, Izhorskaya 13/19, Moscow, 127412 RUSSIA			8. PERFORMING ORGANIZATION REPORT NUMBER	
9. SPONSORING/MONITORING AGENCY NAME(S) AND ADDRESS(ES) USARDSG-UK 223 Old Marylebone Road, London NW1 5TH, UK			10. SPONSORING/MONITORING AGENCY REPORT NUMBER item 0003 (final report)	
11. SUPPLEMENTARY NOTES				
12a. DISTRIBUTION/AVAILABILITY STATEMENT			12b. DISTRIBUTION CODE	
13. ABSTRACT (Maximum 200 words) The samples of as-received Ti-6%Al-4%V alloys of 3 different oxygen contents ranging from 0.1% to 0.24% have been tested in about 50 shock-wave experiments. In the experiments performed, the Hugoniot elastic limit, the spall strength, and the critical diameter for the spall element separation were measured. The peak shock stress was varied from 4 to 75 GPa, the load duration from $\sim 10^{-7}$ s to $\sim 10^{-5}$ s. The VISAR free-surface velocity measurements show a growth by $\sim 20\%$ in the Hugoniot elastic limit of alloys with increasing the oxygen content from 0.105 up to 0.24%. The measurements have not revealed a notable variations in the spall strength magnitudes as a function of the oxygen content. The spall strength grows by ~ 10 to 20% when the load duration decreases by an order of magnitude. The peak stress in shock wave preceding to spall fracture does not influence the spall strength value. The computer simulation of spall experiments was performed with the 1-D Lagrangian code. The description of the elastic-plastic properties is based on the structural Marzing model. Fracture was calculated using the empirical constitutive relationship, which provides quite reasonable description of the spall process.				
14. SUBJECT TERMS TITANIUM, SPALL FRACTURE, HIGH STRAIN RATE DEFORMATION, ENERGY CRITERION OF FRACTURE, EDGE EFFECTS, COMPUTER SIMULATION, FRACTURE MODEL			15. NUMBER OF PAGES 28	
			16. PRICE CODE	
17. SECURITY CLASSIFICATION OF REPORT UNCLASSIFIED	18. SECURITY CLASSIFICATION OF THIS PAGE UNCLASSIFIED	19. SECURITY CLASSIFICATION OF ABSTRACT UNCLASSIFIED	20. LIMITATION OF ABSTRACT UL	

Abstract

The samples of as-received Ti-6%Al-4%V alloys of 3 different oxygen contents ranging from 0.1% to 0.24% have been tested in about 50 shock-wave experiments. In the experiments performed, the Hugoniot elastic limit, the spall strength, and the critical diameter for the spall element separation were measured. The peak shock stress was varied from 4 to 75 GPa, the load duration from $\sim 10^{-7}$ s to $\sim 10^{-5}$ s. The VISAR free-surface velocity measurements show a growth by $\sim 20\%$ in the Hugoniot elastic limit of alloys with increasing the oxygen content from 0.105 up to 0.24%. The measurements have not revealed a notable variations in the spall strength magnitudes as a function of the oxygen content. The spall strength grows by ~ 10 to 20% when the load duration decreases by an order of magnitude. The peak stress in shock wave preceding to spall fracture does not influence the spall strength value. The computer simulation of spall experiments was performed with the 1-D Lagrangian code. The description of the elastic-plastic properties is based on the structural Marzing model. Fracture was calculated using the empirical constitutive relationship, which provides quite reasonable description of the spall process.

Keywords:

TITANIUM, SPALL FRACTURE, HIGH STRAIN RATE DEFORMATION, ENERGY CRITERION OF FRACTURE, EDGE EFFECTS, COMPUTER SIMULATION, FRACTURE MODEL.

Table of Contents

	<u>Page</u>
Introduction.....	1
Theoretical Background of the Method.....	1
Elastic-Plastic and Strength Properties of Titanium	
and Titanium Alloys under Shock-Wave Loading.....	7
Materials and Samples.....	8
Technique.....	9
Results of Measurements.....	11
1-D Computational Study.....	20
Discussion and Conclusion.....	25
References.....	27

INTRODUCTION.

The objective of this project is to study the system of engineering criteria of fracture and fragmentation, including energy criterion of separation of the spall element, and to study the influence of oxygen content in Ti-6Al-4V alloy on the spall strength and the specific energy of spall element separation under shock-wave loading.

Titanium alloys, due to their high strength properties, have a great potential for some armor applications. Pure titanium has a hexagonal crystal structure. At the temperature of 882.5°C the hexagonal α -modification transforms to the body-centered cubic β -modification. In titanium alloys with the additive content more than 5% the transformation temperature can be reduced to the ambient temperature, so those alloys may exist in the β -modification [1]. At high pressure the $\alpha \rightarrow \omega$ phase transformation in titanium was observed by different laboratories both under static [2-4] and dynamic [5] compression. The ω phase has a more open hexagonal structure. The static pressure values range from 2.0 to 7.5 GPa. Factors which are responsible for this scatter were identified [6] as pressure exposure time, sample preparation history, impurity contents, and non-hydrostaticity of the applied pressure. Wave profile measurements showed transition pressures at shock compression of 11.9 [7], 6.0 [8] (both for the commercial grade titanium VT1-0) and 10.4 GPa [9] for electrolytic titanium. Examination of Ti samples recovered after shock compression at low temperatures has shown some amount of the ω -phase at the 9 GPa shock pressure. The ω -fraction increases with increasing peak pressure up to ~25 GPa [5]. The high-pressure transitions was not observed for β and $\alpha+\beta$ titanium alloys.

The ballistic performance of titanium alloy was analyzed and compared the results with rolled steel armor at impact velocities up to 2 km/s in refs. [10-12]. The unique properties of titanium alloys, i.e. uniform hardness and high strength over the total thickness range at low density, result in ballistic performance improvements up to 50-80% on a mass basis as compared to steel with a space effectiveness only about 10% less than steel. The effectiveness is especially high at the impact velocity below ~1 km/s where contribution of the strength properties is more important than purely hydrodynamic effects.

Since the titanium alloys are promising in the armor application, it becomes important to understand better how their dynamic strength properties may be varied depending on the composition and structure. In particular, it is known [1] that under normal conditions the yield stress and tensile strength are growing with increasing the oxygen or nitrogen content in titanium while the ductility goes down. The strength increase reaches the factor of 3 or more at the oxygen content of about 2 at. %. The mechanical properties of titanium alloys are not so sensitive to the oxygen content. On the other hand, a general tendency is that mechanical properties of the materials with low yield stress are more sensitive to the strain rate. To make a correct choice of alloys with highest potential for the armor purposes, we need a systematic study of correlation between the metallurgical characteristics of titanium and titanium alloys and their mechanical properties under impact loading. The planned research work includes measurements of the Hugoniot elastic limits, the spall strength, the work of spall fracture, and the specific energy of spall element separation.

THEORETICAL BACKGROUND OF THE METHOD.

All methods of measurements of tensile stress at spalling are indirect because it is impossible to introduce any sensor into the sample without influence on its resistance to tension. Due to that discrepancies between results of the spall strength measurements by different methods sometimes are very large. The choice of method of investigation which can provide most complete and valid information, as well as understanding of abilities and

limitations of each method are very important.

Measurements of spall strength are based on analysis of the one-dimensional motion of compressible, continuous, condensed media following reflection of a shock pulse by the surface of the body. Figure 1 shows time-distance, ($t-x$), and pressure-particle velocity, ($p-u$), diagrams that illustrate the dynamics of reflection of triangular shock pulse when it encounters a free surface of a body. In the $t-x$ diagram, the shock front trajectory is described by the line OO' . A family of C_+ characteristics represents the unloading wave overtaking the shock front. When the shock front reaches the free surface, the velocity of the latter undergoes a jump from zero up to $u_0 = 2u_s$, where u_s is the particle velocity behind the shock front. The following unloading decreases the free-surface velocity. Reflection of the shock wave by the free surface produces a centered rarefaction wave which is described by a fan of C_- characteristics. The state of particles must satisfy conditions on both the C_+ and C_- characteristics and is determined in the $p-u$ diagram by intersection of Riemann trajectories C_+ describing states of matter along the C_- and C_+ characteristics which pass through a given particle at some given time moment. The maximum tensile stress is reached at each particle as it is traversed by the terminal characteristic of the centered rarefaction wave. So, the peak tensile stress in a spall plane just before the fracture corresponds to the intersection of trajectories $O'K$ and $2K$ in the $p-u$ plane of Fig. 1. Line $O'K$ describes the change of state along the tail C_- -characteristic of the centered rarefaction wave; $2K$ is the trajectory of the change of state along the last of the C_+ -characteristics of the incident wave crossing the spall plane before the fracture.

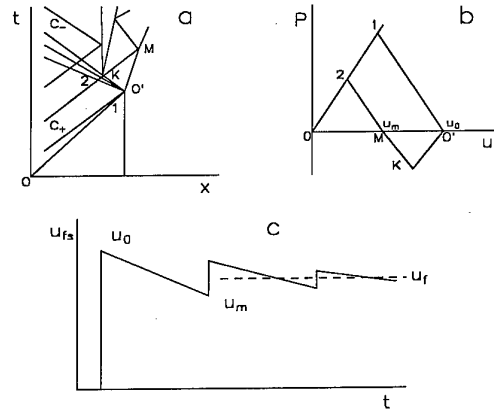


Figure 1. Generation of tensile stresses and wave dynamics at spalling.

Fracture of material allows the tensile stress to decrease rapidly to zero. As a result, a compression wave appears in stretched material adjacent to the spall plane. This wave propagates to the free rear surface. As a result, a so-called spall pulse in the free surface velocity profile, $u_{fs}(t)$ is formed. Subsequent reverberations of the spall pulse between the free surface and spall plane are accompanied by damped oscillations of $u_{fs}(t)$.

The peak velocity, u_0 and the free-surface velocity, u_m , just before the spall pulse, are determined directly from the free surface velocity profile. The tensile stress value just before spalling is then determined by intersection of Riemann trajectories passing through point ($p=0$, $u=u_0$) for C_- and ($p=0$, $u=u_m$) for C_+ . Within the acoustic approach the following linear approximation:

$$\sigma^* = \frac{1}{2} \rho_0 c_0 \Delta u_{fs} \quad (1)$$

is used [13], where $\Delta u_s = u_0 - u_m$ is the so-called "velocity pullback". Dynamic measurements of the spall strength are based on measurements of the velocity pullback. Non-linearity of material compressibility has to be taken into account in the case of high tensile stresses. This can be done by extrapolation of the material isentrope in the $p-u$ plane to the negative pressure region. Really, this correction does not exceed 10% in practical cases.

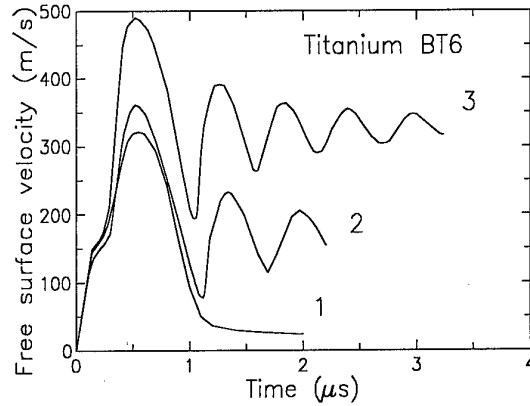


Figure 2. Free surface velocity histories of titanium VT6 samples 10 to 12 mm thick impacted by aluminum flyer plates 2 mm thick with velocity of 445 m/s (profile 1), 600 m/s (2), and 700 m/s (3).

Figure 2 shows examples of measurements of free surface velocity profiles for the titanium alloy VT6 (Ti-6%Al-4%V) [14]. One can see that free surface velocity profile practically replicates the form of the compression pulse in the sample if the load intensity is small (profile 1). The elastic-plastic compression wave and the following complete unloading are recorded. A small velocity hysteresis is explained by hysteresis of the cycle of elastic-plastic deformation. Measurement of the free surface velocity right behind the elastic precursor wave front gives us the Hugoniot elastic limit, σ_{HEL} which is related to the yield stress, Y , through the relationship:

$$Y = 1.5 \sigma_{HEL} (1 - c_b^2 / c_l^2), \quad (2)$$

where c_b and c_l are the bulk and longitudinal sound velocity respectively.

Tensile stresses developed in the body after reflection of the compression pulse by the free surface increase with growth of shock intensity. When the peak tensile stress reaches the fracturing magnitude, the nucleation and growth of cracks is initiated. Then, tensile stresses relax to zero with development of the fracture. As a result, a compressive disturbance called a "spall pulse" appears on the free surface velocity profile. Thereafter wave reverberation is observed within the scab between the free surface and the damage zone. The period of velocity oscillation is a measure of the thickness of the scab. As it was discussed above, the velocity pullback, Δu_{fs} , is a measure of incipient fracture strength of the material. Experiments show that increasing the shock amplitude does not influence the magnitude of Δu_{fs} .

For most solids, the free surface velocity profiles exhibit elastic-plastic properties. There are several sound velocities in the elastic-plastic body. In the case of one-dimensional process weak perturbations propagate with longitudinal sound velocity, c_l , if the deformation is elastic, and with bulk sound velocity, $c_b < c_l$, in the plastic deformation region. We have to decide which sound velocity should be used to calculate the tensile stress at a spalling plane.

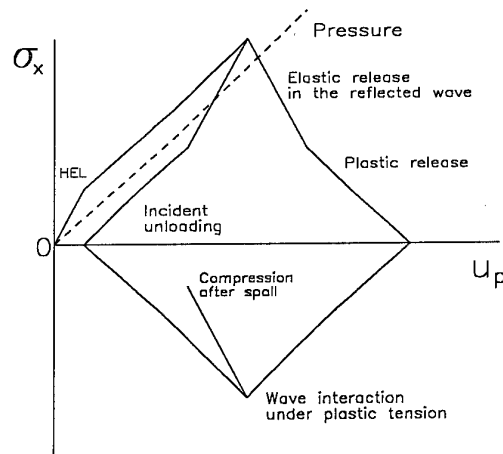


Figure 3. States of an elastic-plastic material at reflection of a compression pulse by the free surface.

Figure 3 shows the diagram of states of axial stress and particle velocity (σ_x, u) for wave interaction when a plane square compressive pulse is reflected by a free surface of the elastic-plastic body. The process of uniaxial compression is elastic until the stress reaches the Hugoniot elastic limit (HEL). The slope of the initial elastic part of Hugoniot below the HEL in these coordinates is $dp/du = \rho c$. The slope in a plastic deformation region above the HEL is equal to ρc_b . Unloading of shock-compressed matter is initially elastic in both the incident and reflected waves. The elastic part of unloading has magnitude equal to two HEL. After that all expansion processes occur in the plastic region.

Thus, if the shock-wave amplitude exceeds the HEL at least two times, tension produced under interaction of rarefaction waves takes place in the plastic deformation region. This means that Riemann's trajectories in the tension region have slopes defined by the bulk compressibility and we have to use the bulk sound velocity for calculation of stress using Eq. 1. On the other hand, the spall pulse is a compression wave which propagates through the extended material and, therefore, must have an elastic precursor. Thus, the spall pulse front propagates with the longitudinal sound velocity whereas the rarefaction plastic wave ahead of it propagates with the bulk sound velocity (Fig. 4). As a result, the compression wave, which appears due to the stress relaxation at fracture, overtakes the release part of the incident shock pulse and measured velocity, u_m , exceeds the value which we should use in Eq. 1 for calculation of stress.

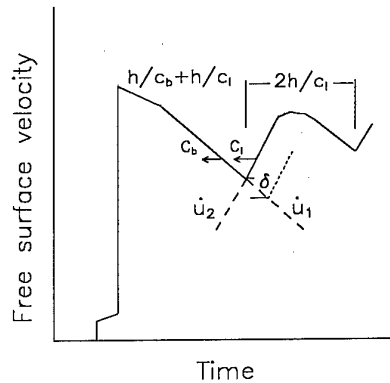


Figure 4. Distortion of the wave profile resulting from the different propagation velocity of the unloading wave and the spall pulse front in an elastic-plastic body.

The corrected expression for calculation of tensile stress before spalling is

$$\sigma^* = \frac{1}{2} \rho_0 c_b (\Delta u_s + \delta), \quad (3)$$

where δ is a correction for the profile distortion due to the elastic-plastic properties of the material. Taking into account the velocity gradients ahead of the spall pulse, \dot{u}_1 , and the gradient in its front, \dot{u}_2 , the correction magnitude is estimated as

$$\delta = \left(\frac{h}{c_b} - \frac{h}{c_t} \right) \frac{|\dot{u}_1 \dot{u}_2|}{|\dot{u}_1| + |\dot{u}_2|}, \quad (4)$$

where h is the thickness of spall plate.

Obviously, experiments must be designed to provide the smallest correction magnitude. It can be shown that correction value is reduced to ~10% of Δu_{fs} in the case of an incident load pulse of triangular form. In typical experiments the shock load is created in samples by impact of flyer plate. In this case, pressure and particle velocity profiles keep an approximately rectangular form until the distance of propagation reaches ~5 thicknesses of impactor. After that, the unloading wave overtakes the shock front and the load pulse becomes triangular. Thus, the optimal ratio of a sample thickness to the impactor thickness must exceed 5 to have the smallest correction and smallest possible error of the spall strength value.

Correctness of determination of fracturing stress using the free-surface velocity profiles has been multiply confirmed by experiments with intensities of shock load close to the spall strength magnitude. A spall pulse was not recorded in these experiments at the peak load stress below the spall strength but it appeared in the velocity profiles with increasing load above the spall strength. Then the velocity pullback value was practically conserved at following increasing shock load. Careful comparison of instrumental measurements with results of microscopical examination of tested samples shows the fracture just nucleates at load stress magnitude equal to σ^* .

Spall strength value only defines conditions for damage nucleation; it does not exhaustively characterize the material response. Development and completion of the spall process occur at reduced stress, but require consumption of additional energy for the growth of flaws and plastic deformation of material around them. When the initial load pulse is short, fracture, once started, may not proceed to complete separation of the body into distinct parts.

An energy criterion [15, 16, 17] defines the possibility of complete rupture through comparison of the work of fracture and the amount of energy stored in the body. The work of fracture is the energy expended per unit cross-section area of the body in the course of fragmentation. In reality the dissipation of energy due to the fracture takes place in some layer of finite thickness and, therefore, the work of fracture, generally speaking, rises with increasing size of the failed zone.

Estimation of the energy dissipated in the course of a fracture process can be based on either of two kinds of experiments. The first kinds of experiments determines the critical impact velocity which produces spall for given thickness of impactor and sample. Using the critical impact velocity thus determined, and parameters of the experiment, the energy dissipated is determined through consideration of the balance of energy and momentum as

$$E_d = \rho h_i v^2 (1 - h_i / h_t) / 2, \quad (5)$$

where v is the impact velocity, and h_i and h_t are thickness of the impactor and target, respectively. The dissipated energy thus calculated is an upper bound for the magnitude of the work of fracture. The second kind of experiment involves measurements of a free-surface velocity profile. The loss of kinetic energy of the spall plate as it decelerates during the spall process can be inferred from this profile and can be used for estimation of the work of dynamic fracture.

The fracture stress and work of fracture describe the strength properties of the materials when subjected to one-dimensional dynamic tension. However, these two parameters are not enough to predict the occurrence of complete separation of scab or to estimate its velocity after the separation.

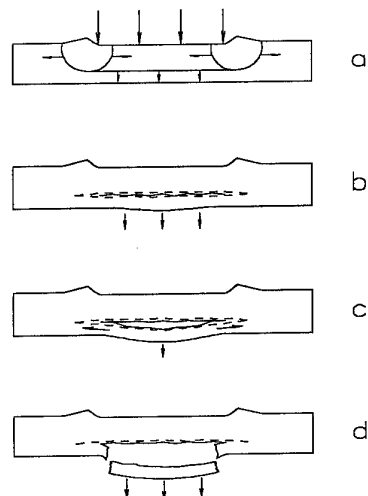


Figure 5. Edge effects at spallation

Figure 5 shows the evolution of spalling in a limited area of a plane body [18]. The incident shock is attenuated not only by the axial unloading waves but also by the lateral release. At reflection of this attenuated load pulse from the free surface the tensile stresses and energy stored, which are sufficient for the complete fracture, are realized only near the axis. Thus, the fracture of the body by the plane wave is limited to some inner region. The subsequent evolution of the process is determined by the kinetic energy stored in the scabbed element.

The inertial motion of the scabbed layer is decelerated by bonding forces in the periphery of the scab. The scab motion can even be stopped by the edge effects. Additional work is necessary for plastic deformation and fracture along the edge of a spall element. The work of edge deformation and fracture is proportional to the length of the spall element perimeter, whereas the value of energy stored in the element is proportional to its area. The ratio of these two values increases with reduction of the spall element radius. In the case of small radius, development of spalling can be stopped at some intermediate stage and the spall element remains connected to the main body. Investigation of spalling with spall elements of different radii allows us to determine a critical stored energy value for complete separation of scab. This variation of the spall element radius can be arranged through varying of the impact area radius or by placement of a limiting ring on the rear surface of the sample.

ELASTIC-PLASTIC AND STRENGTH PROPERTIES OF TITANIUM AND TITANIUM ALLOYS UNDER SHOCK-WAVE LOADING

The spall strength and Hugoniot elastic limits of titanium and titanium alloys were investigated in refs. [14, 19, 20, 21, 22]. Figures 2, 6, 7, 8 show the free-surface velocity profiles measured for pure titanium and titanium alloys in our previous studies.

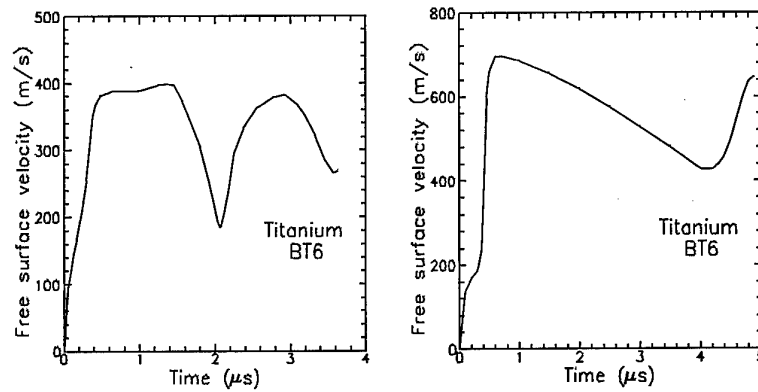


Figure 6. The free-surface velocity profiles for Ti-6%Al-4%V alloy at loading by aluminum impactor 4 mm thick and by detonation of the explosive lens [14].

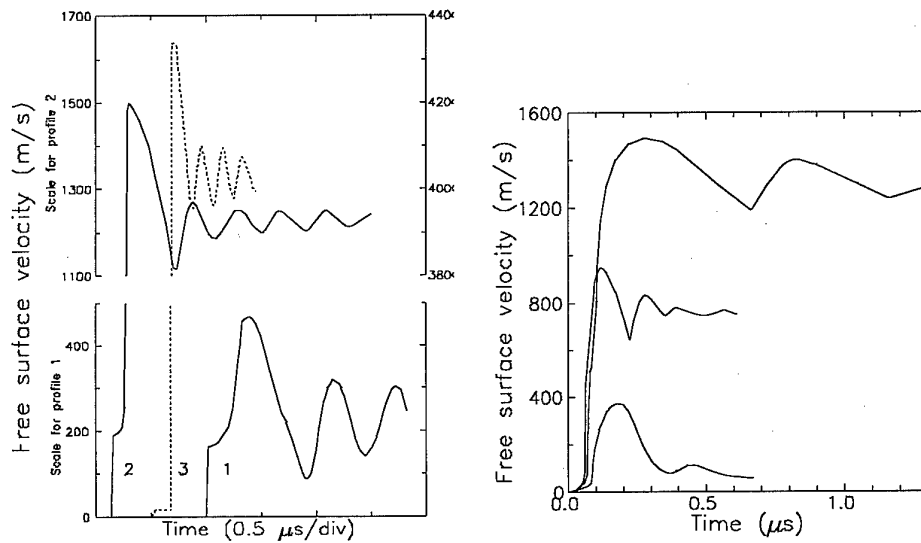


Figure 7. Free-surface velocity profiles for the VT8 (TiAl_{6.5}Mo_{3.5}(Si_{0.3})) alloy. Impact by aluminum flyer plate 2 mm thick with velocity of 700 m/s (profile 1), 1900 m/s (2), and 5300 m/s (3) [20].

Figure 8. The free-surface velocity profiles for titanium of high purity [19].

Results of measurements of the spall strength and the Hugoniot elastic limits are summarized in Table 1. As it can be seen from the Table, the spall strength of the Ti6Al4V alloy was measured by many authors and equals or even exceeds the spall strength of armor steels. A scatter in this parameter from 3.5 to 5.1 GPa is, perhaps, a result of uncontrolled

initial state of the material. Another reason of the discrepancy may be related to the material texture: it is known the strength in rolling direction may significantly exceed the stress value under loading in transversal direction. Post-test metallurgical examination of the titanium samples [27] have shown viscous character of the spall fracture which occurs through nucleation and growth of nearly spherical pores. Unlike to other metals, the stress threshold of spall nucleation for titanium (~ 3 GPa) is in a good agreement with the spall strength value measured from the free surface velocity profiles.

Table 1. Hugoniot elastic limit and spall strength of titanium and titanium alloys measured using the free surface velocity histories.

Material	HEL (Yield stress), GPa	Strain Rate at unloading, s^{-1}	Spall Strength, GPa	Spall Thickness, mm	Ref.
Pure titanium			3.1 to 3.8	2 to 2.6	[24]
Titanium of high purity		$(1.1-3.2) \cdot 10^5$	3.7 ± 0.05		[19]
		$(1.4-5) \cdot 10^6$	5.6 to 6.3		
Titanium alloy VT6 (Ti6Al4V), sheet	2.0 (0.9)	$8.3 \cdot 10^3$	3.4 ± 0.2	9.8	[14]
		$6.2 \cdot 10^4$	3.5 ± 0.2	1.8	
		$8 \cdot 10^4$	3.7 ± 0.2	1.7	
Titanium alloy Ti 6Al 4V			4.1 to 5		[21]
Titanium alloy Ti 6Al 4V	2.8				[22]
Titanium alloy Ti 6Al 4V	2.3(1.21)		5.08	~ 3	[23]
Titanium alloy Ti 6Al 4V			3.6 to 4.2	2.2 to 2.6	[24]
Titanium alloy Ti 6Al 4V		$(1.7-2) \cdot 10^5$	4.7 to 4.9		[26]
Titanium VT5-1 (TiAl5Sn2.5), sheet	2.7(1.25)	$1.3 \cdot 10^5$	4.16 ± 0.1	1.9	[25]
Titanium alloy VT8 (TiAl6.5Mo3.5(Si0.3)), rod	2.45(1.15)	$7.5 \cdot 10^4$	4.65 ± 0.3	1.65	[20]

It has been shown [20] the spall strength of titanium alloy does not depend on the peak pressure up to 70 GPa in shock wave preceding to spall fracture. Measurements of the specific energy of the spall element separation performed for the VT5-1 titanium alloy [18] have shown this value ($1.3 \cdot 10^6$ J/m²) much exceeds the work of internal spall fracture ($2.5 \cdot 10^5$ J/m²) as a result of contribution of the work for plastic deformation on a periphery of the spall element.

MATERIALS AND SAMPLES

In the framework of this project, plate impact experiments with three kinds of samples of Ti-6Al-4V alloy with different oxygen contents have been performed. The compositions and mechanical properties of the three ingots tested are listed in the Table 2.

Table 2. Compositions and mechanical properties of the materials tested.

Ingot No	Composition, weight %						Mechanical properties			
	C	N	Fe	Al	V	O	Ultimate Tensile Strength (GPa) L/T	0.2% Yield Strength (Gpa) L/T	Elong., % L/T	Reduct. in area, % L/T
58784	0.02	0.013	0.18	5.80	3.78	0.105	0.89 0.93	0.8 0.84	14 12	33 30.5
G3540	0.012	0.006	0.156	6.16	3.89	0.198	0.97 1.03	0.88 0.96	16 15	27 31
64291	0.035	0.011	0.24	6.33	3.95	0.24	1.01 1.05	0.89 0.95	13 13	28 23

The samples have been cut out of rolled plate ingots of 38 to 40 mm in thickness. The processing for the three plates were follows:

Ingot 58784 was straight rolled above β -transus, annealed at 788°C for 30 min., and air-cooled. The microstructure is acicular α + β phase and prior β grain boundaries.

Ingot G3540 was cross rolled below β -transus, annealed at 760°C for 60 min., and air-cooled. The microstructure consists of equiaxial α , acicular α , and banded α phases in transformed β phase. No evidence of segregation or overheating was observed.

Ingot 64291 was straight rolled above β -transus, annealed at 788 for 30 min., and air-cooled.

Thus, the static mechanical properties of G3540 and 64291 ingots are very close, while the 58784 ingot shows the ultimate tensile strength and the yield strength lower by ~10% than the two others ingots.

The samples were 80×60 mm in plane and 2 to 15 mm in thickness and had lapped surfaces.

For analyzing the experimental data we used the Hugoniot relationship between the shock velocity, U_s , and the particle velocity, u_p , of the alloy in form $U_s = 5.05 + 1.034u_p$ (km/s) at the incident density of 4.42 g/cm³ and the longitudinal sound velocity $c_l = 6.21$ km/s.

TECHNIQUE

To investigate the strength properties of condensed matter under shock-wave loading we have to be able to create plane shock pulses in our samples and to measure an evolution of these pulses inside the sample. Plane shock waves for spall strength measurements were created by impacting the sample to be studied with a flyer plate or by detonating an explosive plane wave generator in contact with it.

Figure 9 shows one of a typical arrangement of an explosive launching device which was used to accelerate the aluminum impactor plate 2 mm thick up to velocity of 5.3 km/s. The impactor remains flat over its central part despite the fact that the pressure on the periphery of the explosive charge drops faster than on its axis because of the radial expansion of the explosion products. For this the pressure pulse at the impactor edge is corrected by the guard

ring. Due to reflection of the detonation wave from the guard ring, the pressure on the periphery rises for short time what produces additional inflow of the explosion products into the gap above the impactor.

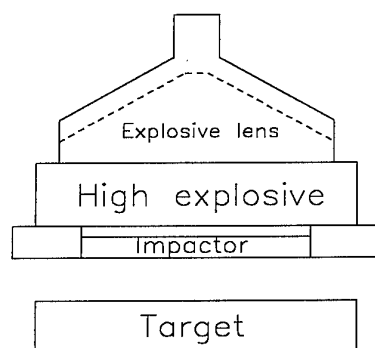


Figure 9. Experimental configuration for using explosives to launch a flyer plate at high velocity.

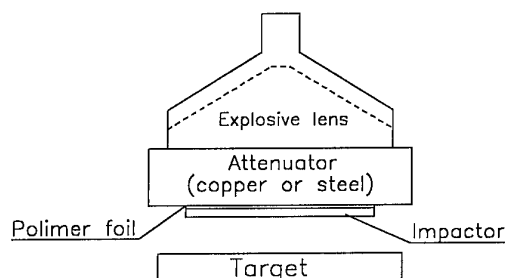


Figure 10. Experimental configuration for using explosives to launch a flyer plate at low velocity.

It is difficult to attain an impactor velocity below 1 km/s using direct launching by the explosion products. Figure 10 shows another explosive facility designed for low-velocity launching. Detonation of explosive charge produces a plane shock wave in the intermediate plate or attenuator with high dynamic impedance. A flyer plate which has been placed behind the attenuator has lower dynamic impedance. Due to that, when the shock wave arrives on the free rear surface of the flyer plate, the latter acquires a velocity that is higher than that of the intermediate plate. Thus the flyer plate is separated from the intermediate plate. A soft polyethylene gasket is used to prevent damage to the impactor as a result of rarefaction wave reflection from rigid attenuator. This device is also attractive in that it can launch very thin impactors, such as foils or films, used to produce short shock pulses.

The free-surface velocity profiles were recorded with the VISAR laser Doppler velocimeter [28,29] shown in Figure 11. The high space resolution of the laser techniques is due to the fact that the laser beam is focused down to a spot ~ 0.1 mm in diameter on the target surface.

The output VISAR signals were recorded with a high-frequency digital oscillograph Tektronix TDS 744A. The accuracy of the velocity measurements with VISAR is $\sim 1\text{-}2\%$ or less, the time resolution was ~ 2 ns.

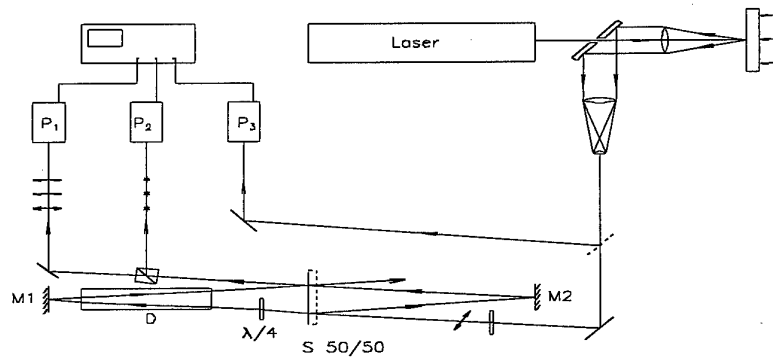


Figure 11. Schematic of a VISAR two-beam laser Doppler velocimeter [28,29].

RESULTS OF MEASUREMENTS

The samples of Ti-6%Al-4%V alloys of 3 different oxygen contents have been tested in about 50 shock-wave experiments. Table 3 summarizes the VISAR experiments with the free surface velocity history measurements. The peak shock stress was varied from 4 to 75 GPa, the load duration from $\sim 10^{-7}$ s to $\sim 10^{-5}$ s, and the sample thickness from 2 to 24 mm. Figures 12 to 15 present the typical free surface velocity profiles which have been recorded for samples of three different ingot plates at the same experimental conditions. The recorded elastic precursor waves correspond to average magnitudes of the Hugoniot elastic limit (HEL) of 2.2 ± 0.1 GPa for the 58784 ingot (0.105% O_2), 2.6 ± 0.1 GPa for 64291 (0.24% O_2), and 2.5 ± 0.1 GPa for G3540 (0.198% O_2). These values correspond to the yield stresses $Y = 1.5 \sigma_{HEL} (1 - c_b^2/c_l^2)$ of 1.12 GPa, 1.32 GPa, and 1.27 GPa respectively. These results confirm the oxygen content influence on the dynamic yield strength of the titanium alloy. At low and moderate peak shock stresses the material of ingot 64291 with the maximum oxygen content exhibit a greatest rise time of the plastic shock wave that indicates a slowest stress relaxation. The growth of velocity (and, consequently, stress) behind the elastic precursor front can be an evidence of both the slow stress relaxation or the strain hardening. Unfortunately, reproducibility of the samples was not high enough to analyze the elastic precursor decay. As a result of the greater elastic limit and relaxation time the shock pulses of moderate (< 10 GPa) intensity decay faster in the alloy with 0.24% of the oxygen content. The difference in shock wave decay was not observed when the peak shock stress was increased up to 18 GPa and higher.

Most of the free-surface velocity profiles exhibit a steep front of the spall pulses. This means a brittle character of fracture with a rapid damage growth. The fracturing stresses at spalling were calculated through the velocity pullback value using relationships (3), (4). The results are mentioned in the Table 3 and shown in Fig. 16. Within a scatter of the experimental data the dynamic strength is practically the same for all three kinds of the material and grows by ~ 10 to 20% when the load duration decreases by two orders of magnitude. The peak stress in shock wave preceding to spall fracture does not influence the spall strength value.

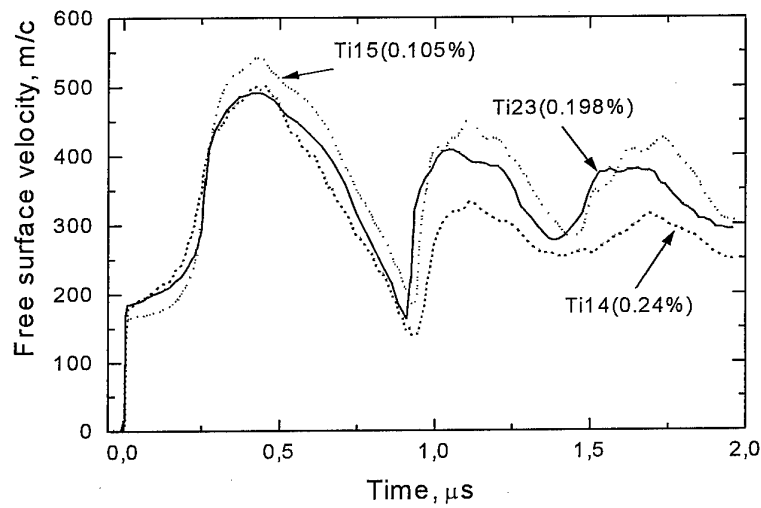


Figure 12. The free surface velocity profiles generated in Ti-6%Al-4%V samples by impact of the aluminum flyer plate 2 mm thick at 700 m/s of the impact velocity.

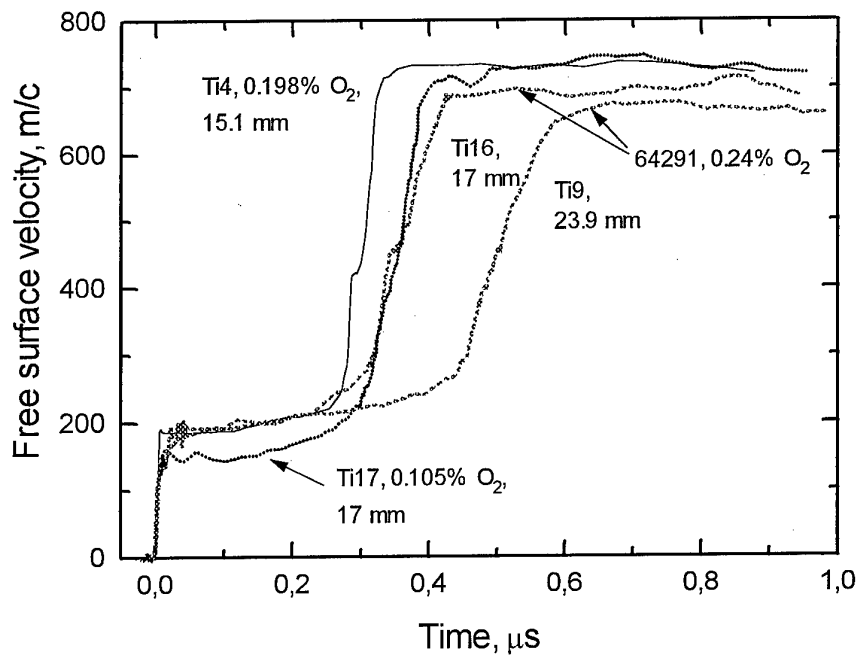


Figure 13. The front portions of free surface velocity histories measured for thick samples.

Table 3. Experimental conditions and results of VISAR experiment with Ti-6%Al-4%V alloys of 3 different oxygen contents.

Shot num.	Loading Conditions	Sample Thickness, mm	Peak Stress, GPa	$\frac{\dot{V}}{V_0}, s^{-1}$	Spall thick. (mm)	Spall Strength (GPa)	HEL, GPa
<i>Ingot 58784, 0.105%O₂</i>							
Ti15	Al impactor 2 mm, 0.7 km/s	10.09	6.4	$9.1 \cdot 10^4$	1.55	4.31	2.29
Ti17	Detonation of explosive lens	17	8.85	$1.0 \cdot 10^4$	10.6	4.1±0.3	2.0
Ti18	Al 0.4 mm, 0.6 km/s	1.88	6.1	$5.25 \cdot 10^5$	0.34	4.58	2.28
Ti19	Al 2 mm, 1.9 km/s	10.06	18.2	$1.2 \cdot 10^5$	1.15	4.44	2.25
Ti20	Al 2mm, 5.3 km/s	9.88	70	$1.7 \cdot 10^5$	0.42	4.6	—
<i>Ingot 64291, 0.24%O₂</i>							
Ti8	Al 2 mm, 0.7 km/s	10.2	5.9	$8.0 \cdot 10^4$	1.66	4.1	2.52
Ti9	Detonation of explosive lens	23.85				lateral unloading	2.50
Ti10	Al 2 mm, 1.9 km/s	9.98	18.6	$1.2 \cdot 10^5$	1.15	4.3	2.56
Ti11	Al 2 mm, 5.3 km/s	10.09	73	$1.7 \cdot 10^5$	0.46	4.6	—
Ti12	Al 0.4 mm, 0.6 km/s	2.4	4.14	$2.0 \cdot 10^5$	0.65	no spall	2.59
Ti13*	Al 0.4 mm, 0.6 km/s	1.94	5.6	$6.5 \cdot 10^5$	0.32	4.8	3.20
Ti14	Al 2 mm, 0.7 km/s	10.12	5.9	$8.0 \cdot 10^4$	1.6	4.27	2.47
Ti16	Detonation of explosive lens	17.01	8.5				2.45
<i>Ingot G3540, 0.198%O₂</i>							
Ti1*	Al 2 mm, 0.7 km/s	6.6	6.2	$1.5 \cdot 10^5$	1.76	4.45	2.47
Ti2	Al 2 mm, 0.7 km/s	8.2	6.3	$1.2 \cdot 10^5$	1.75	4.33	2.55
Ti3	Al 2 mm, 0.7 km/s	10.0	6.1	$1.2 \cdot 10^5$	1.61	4.42	2.6
Ti4	Detonation of explosive lens	15.1	8.8	$1.1 \cdot 10^4$	10.4	3.8±0.3	2.53
Ti5	Al 2 mm, 1.9 km/s	10.1	18.3	$1.2 \cdot 10^5$	1.1	4.3	2.5
Ti6	Al 2 mm, 5.3 km/s	10.1	77	$1.7 \cdot 10^5$	0.43	4.3	—
Ti7*	Al 0.4 mm, 0.6 km/s	2.1	5.4	$3.8 \cdot 10^5$	0.31	4.34	2.1
Ti22	Al 2 mm, 1.3 km/s	9.85	11.9	$1.2 \cdot 10^5$	1.32	4.3	2.47
Ti23	Al 2 mm, 0.7 km/s	10.02	5.8	10^5	1.62	4.1	2.52

* - Samples from middle section of the original titanium plate

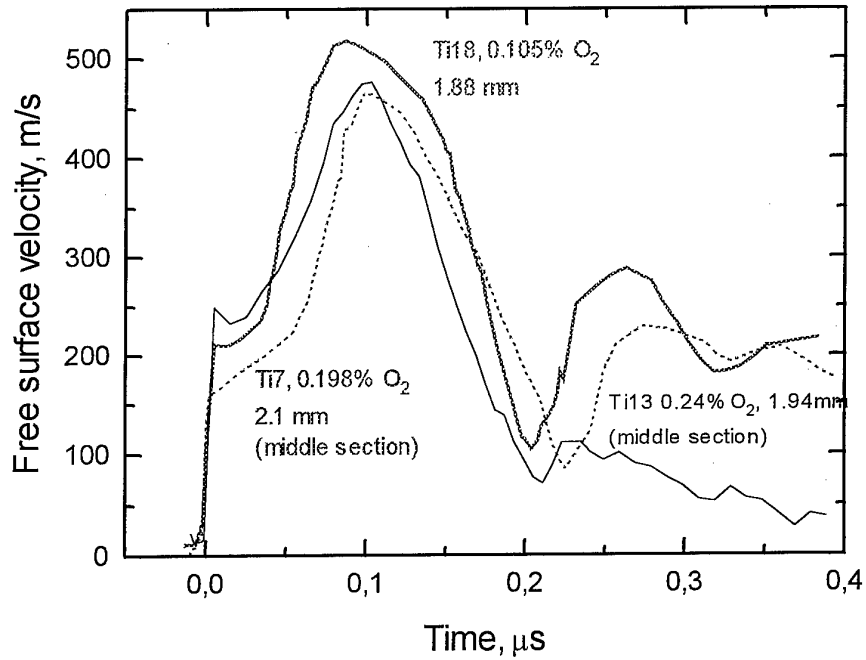


Figure 14. The free surface velocity profiles generated in Ti-6%Al-4%V samples by impact of the aluminum flyer plate 0.4 mm thick at 600 m/s of the impact velocity.

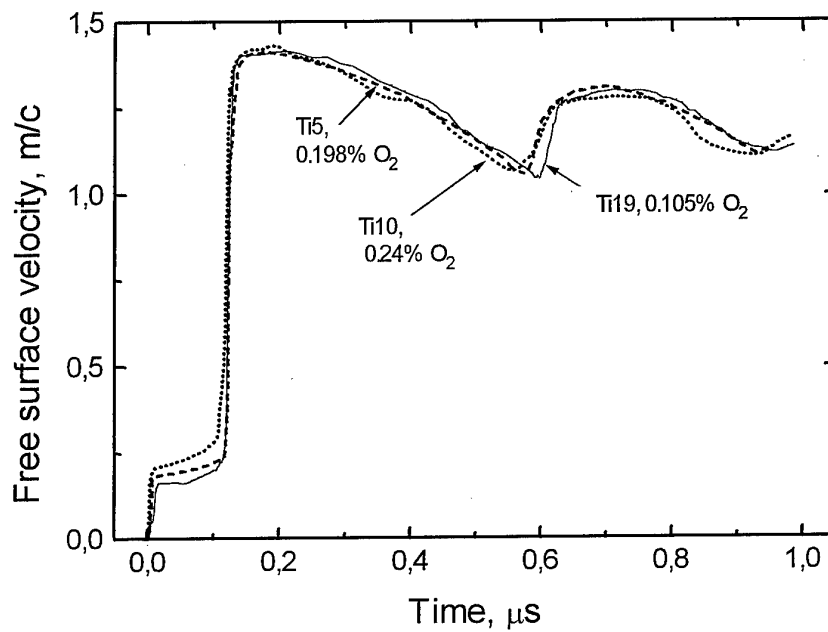


Figure 15. The free surface velocity profiles generated in Ti-6%Al-4%V samples by impact of the aluminum flyer plate 2 mm thick at 1900 m/s of the impact velocity.

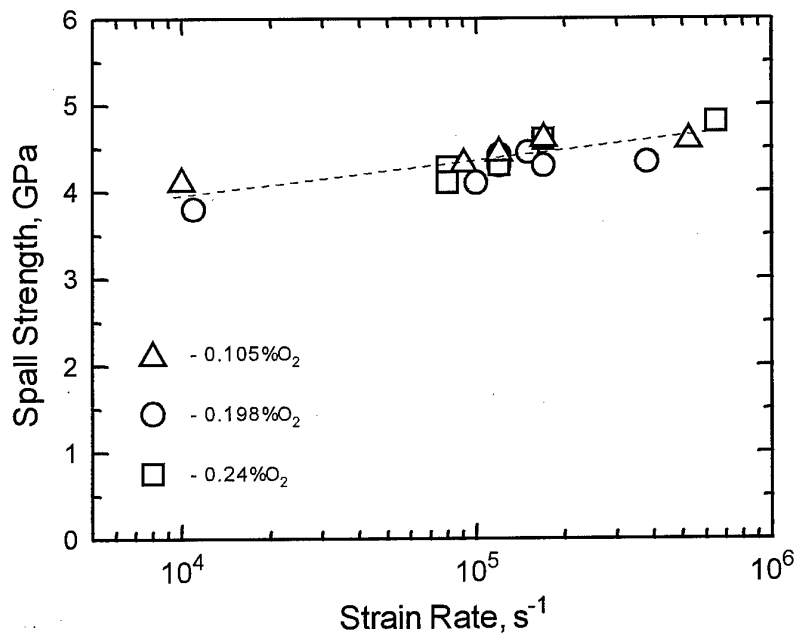


Figure 16. Results of the spall strength measurements as a function of rarefaction rate at unloading in the incident shock pulse.

The inertial motion of the scabbed layer is decelerated by bonding forces in the periphery of the scab. Additional work is necessary for plastic deformation and fracture along the edge of a spall element. The work of edge deformation and fracture is proportional to the length of the spall element perimeter, whereas the value of energy stored in the element is proportional to its area. The edge effects of spall fracture were investigated mainly at the impact conditions (aluminum plate impactor of 2 mm in thickness at 700 ± 20 m/s of the impact velocity) corresponding to ~ 6 GPa of the peak shock stress for all three materials. The variation of the spall element radius was arranged by placement of a limiting ring on the rear surface of the sample as it is shown in Fig. 17.

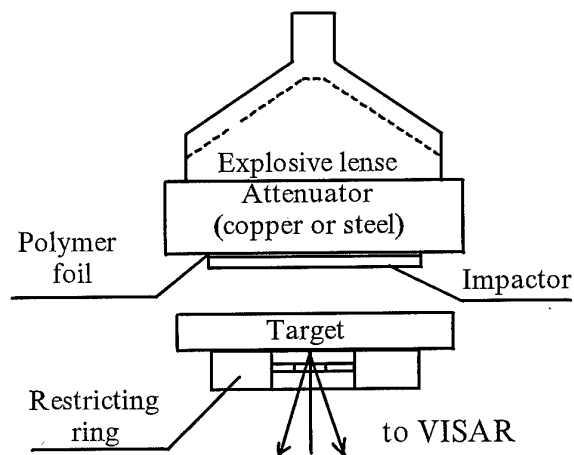


Figure 17. Scheme of experiments to study the edge effects of spall fracture.

Figure 18 illustrates the scheme of recovering the tested samples. Photos of the recovered samples are presented in Figs. 19 to 21. The results of these experiments are summarized in the Table 4.

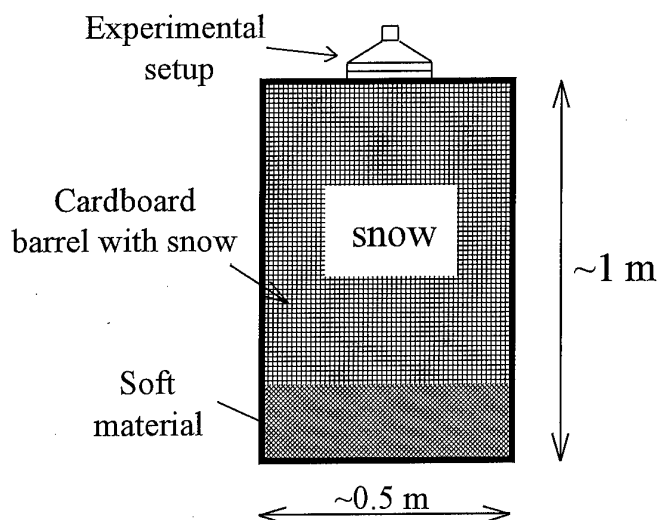


Figure 18. The scheme of soft recovering the tested samples.

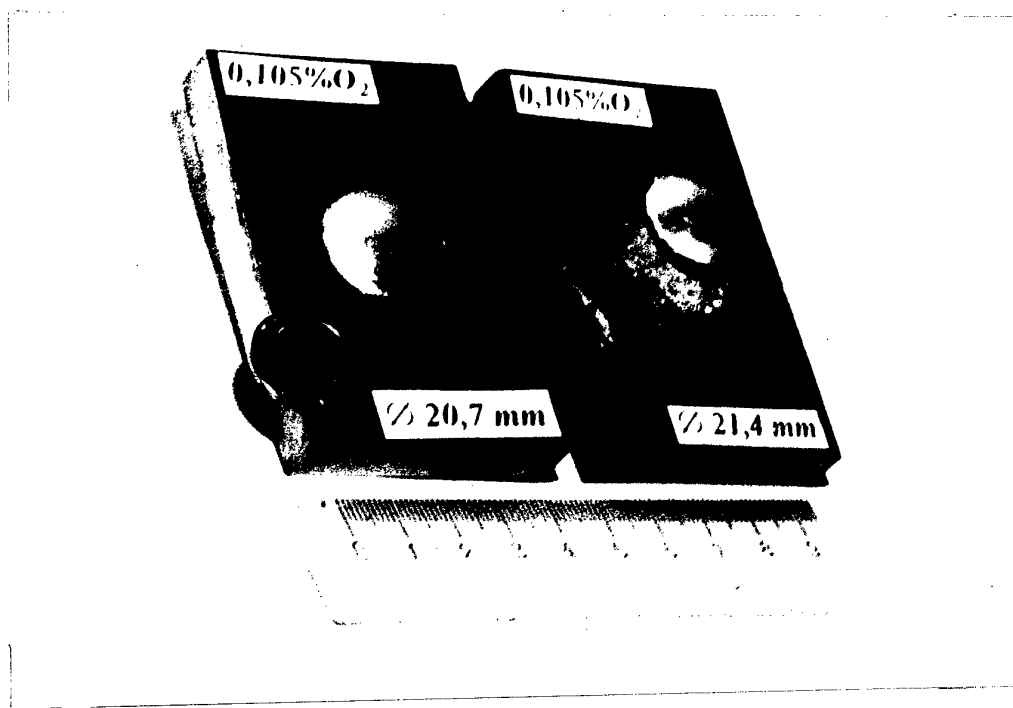


Figure 19. Rear surfaces of samples of 58784 ingot recovered after the tests on edge effects of spall fracture.

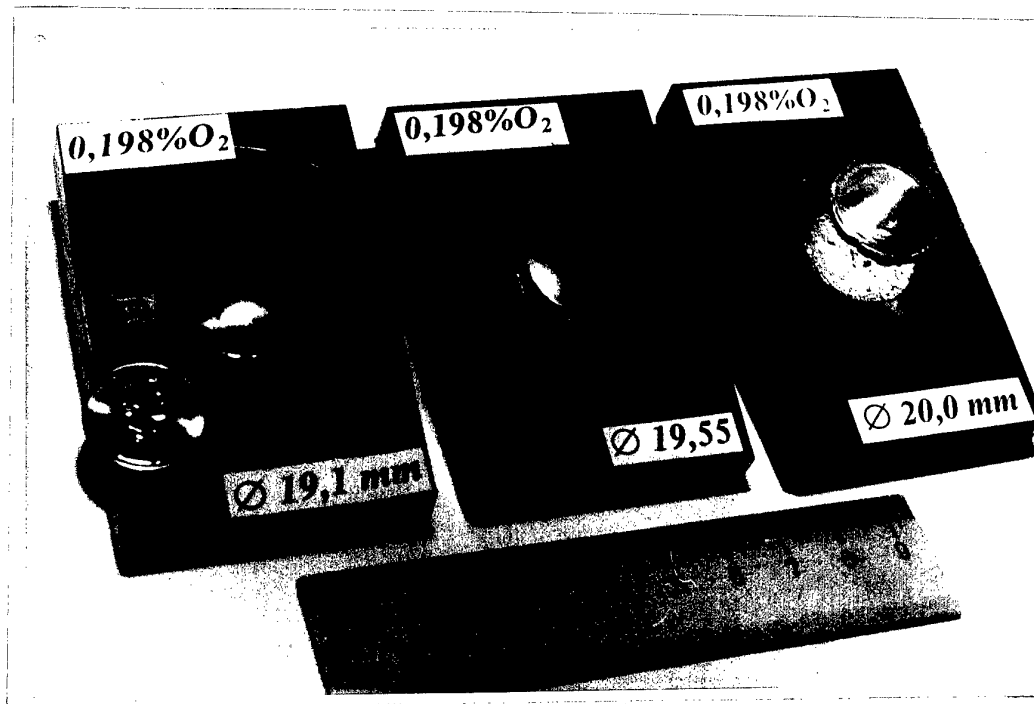


Figure 20. Rear surfaces of samples of G3540 ingot recovered after the tests on edge effects of spall fracture.

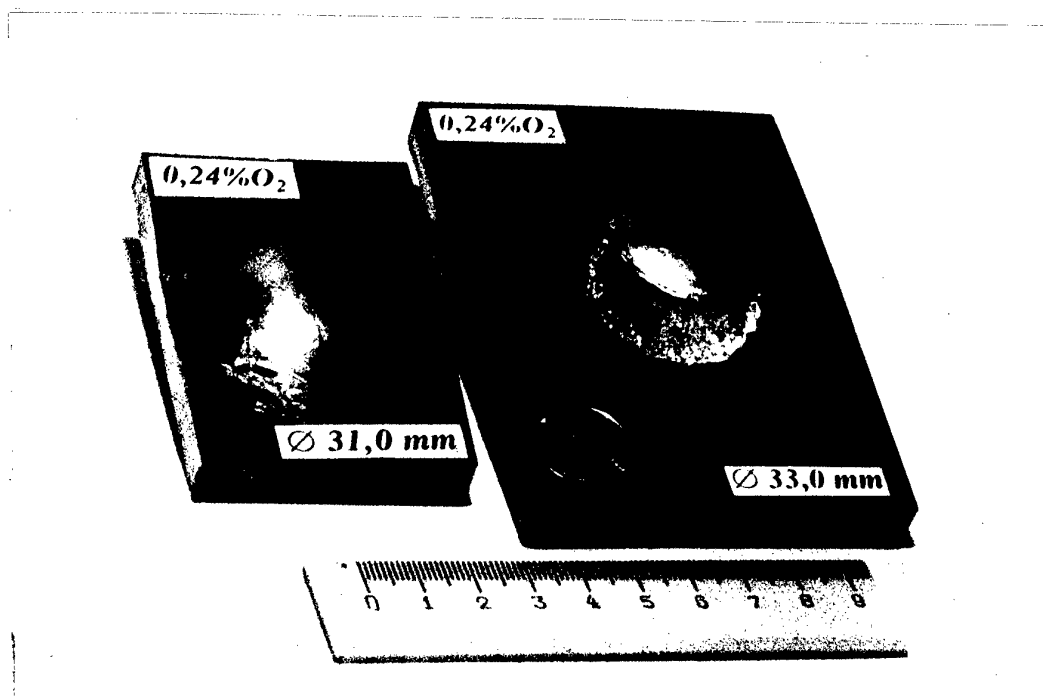


Figure 21. Rear surfaces of samples of 64291 ingot recovered after the tests on edge effects of spall fracture. Impact velocities 700 m/s.

Interpretation of these experiments was done in the following way. From the measurements of free surface velocity histories the work of spall fracture and the residual kinetic energy of the spall plate were determined. The work of spall fracture was determined as a deficit of specific kinetic energy of the spall plate, $E_i - E_{sp}$, where E_i is the specific energy introduced into the spall plate during the incident velocity pulse and E_{sp} is the specific residual kinetic energy of the spall plate. For this the relationship was used:

$$E_i - E_{sp} = 0.5 \rho h (u_i^2 - u_{sp}^2),$$

where ρ and h are the alloy density and the spall thickness respectively, u_i and u_{sp} are average velocity for the first velocity pulse and for following velocity oscillations in the free surface velocity profiles. Both these values were calculated for the same thickness of the spall plate as the distance passed during the velocity oscillation divided by the oscillation period.

The residual energy, E_{spe} , of spall element of critical diameter was calculated using the formula

$$E_{spe} = 0.5 \rho h u_{sp}^2 \pi D_c^2 / 4,$$

where D_c is the critical diameter of the spall element separation. To characterize the material we determined the specific energy of the spall element separation, E_b , as the E_{spe} value divided by the area of periphery of the critical spall element:

$$E_b = E_{spe} / \pi D_c h.$$

Using the result of shot Ti15 we have found for the ingot 58784 (0.105% O₂) $u_i = 420.5$ m/s, $u_{sp} = 368$ m/s, and $E_i - E_{sp} = 1.42 \cdot 10^5$ J/m². Using the critical diameter value of 20.7 mm, we have found $E_{spe} = 152.9$ J and $E_b = 1.52 \cdot 10^6$ J/m². In other word, as a result of larger deformation along the periphery of the spall element, the specific energy of the spall element separation exceeds the specific work of spall fracture by an order of magnitude.

Using the result of shot Ti14 we have found for the ingot 64291 (0.24% O₂) $u_i = 369.4$ m/s, $u_{sp} = 279.2$ m/s, and $E_i - E_{sp} = 2.06 \cdot 10^5$ J/m². Using the critical diameter value of 34 mm, we have found $E_{spe} = 250.5$ J and $E_b = 1.46 \cdot 10^6$ J/m² which is even lower than this value for softer alloy.

Using the result of shot Ti23 we have found for the ingot G3540 (0.198% O₂) $u_i = 391.4$ m/s, $u_{sp} = 342.5$ m/s, and $E_i - E_{sp} = 1.3 \cdot 10^5$ J/m². Using the critical diameter value of 19.55 mm, we have found $E_{spe} = 126$ J and $E_b = 1.27 \cdot 10^6$ J/m².

To verify the validity of criterion of spall element separation, some limited amount of experiments with limited spall area have been done at a higher impact velocity of 1.3 km/s. The results which are presented in the Table 4 show that the critical diameter of spall element separation is less than 6 mm. Meanwhile, using the results of previous evaluations we are estimating the critical diameter value for G3540 as 3.6 mm.

Table 4. Results of determining the critical diameter of spall element separation.

<i>Ingot 58784, 0.105%O₂</i>					
N	Loading	h_{smpl} , mm	$h_{\text{lim.plate}}$, mm	\varnothing spall zone	Comments
1(21)	Al 2 mm (0.7 km/s)	10.01	20	20.2	no separation
2(22)	—	10.04	20	22.6	compl. separation
3(23)	—	10.5	20	21.4	compl. separation
4(27)	—	10.05	20	20.7	critical diam. for sep.
<i>Ingot 64291, 0.24%O₂</i>					
1(15)	Al 2 mm (0.7 km/s)	10.1	20	25	no separation
2(16)	—	10.06	20	28	no separation
3(17)	—	10.04	20	31	no separation
4(18)	—	10.16	20	40	compl. separation
5(19)	—	10.12	20	35	compl. separation
6(20)	—	10.17	20	34	critical diam. for sep.
1(43)	Al 2 mm (1.3 km/s)	9.58	20	15	compl. separation
2(44)	—	9.58	20	10	compl. separation
3(47)	—	9.52	20	6	compl. separation
<i>Ingot G3540, 0.198%O₂</i>					
1(5)	Al 2 mm (0.7 km/s)	10.2	20	20	compl. separation
2(6)	—	10.2	15	17.7	no separation
3(7)	—	10.7	25	18.5	no separation
4(8)	—	10.7	15	19.1	no separation
5(9)	—	10.1	15	19.55	critical diam. for sep.
1(40)	Al 2 mm (1.3 km/s)	9.8	20	15.15	compl. separation
2(41)	—	9.91	20	12.5	compl. separation
3(42)	—	9.94	20	10	compl. separation

1-D COMPUTATIONAL STUDY.

Empirical data on the resistance to dynamic fracture should be generalized by a fracture model or constitutive relationship that can be used for computer simulation of impact phenomena. The relationship should be efficient over a wide range of load duration.

The computer simulation of spall experiments was performed with the 1-D Lagrangian code. To analyze the spall phenomena using computer simulations we need a reasonable model of the elastic-plastic response of material tested which would provide the same load conditions at spalling in simulations as it takes a place in the experiments. One should say that after many years of studying the mechanical properties of materials under shock-wave loading a description of the elastic-plastic response is still a non-trivial task. Figure 22 shows an experimental free-surface velocity history and results of computer simulations using well-known simple models.

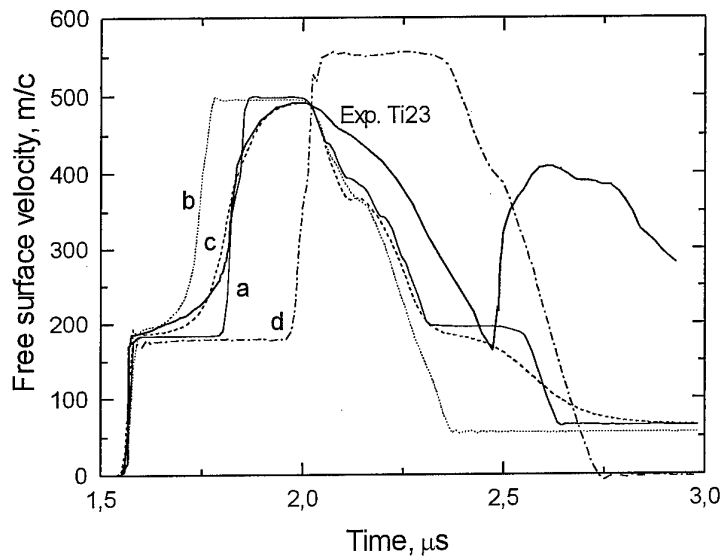


Figure 22. Results of computer simulations of the impact loading of Ti-6%Al-4%V samples. The free-surface velocity profile "a" has been calculated using a model of ideal elastic-plastic body. Profile "b" is the result of simulation for a strain-hardening elastic-plastic body; profile "c" is the result of simulation for an elastic-viscous-plastic body; and profile "d" is the result of simulation for elastic-isotropic body. Thick line presents the experimental data.

With a model of ideal elastic-plastic body we have received a two-wave structure of the load pulse both at compression and unloading. The compression portion of the load pulse in this case looks like two steep steps with a plateau between them while the measured velocity history demonstrates a rise right behind the elastic precursor front and the plastic wave with a measurable rise time. It has been shown earlier [30] that the strain hardening presented as $Y=Y_0+Y'\gamma_p^n$, where Y is the yield stress, γ_p is the plastic strain, and Y_0 , Y' , n are constants, leads to the stress and particle velocity rise behind the elastic precursor front. The simulation for the strain-hardening elastic-plastic body gives indeed the rise behind the elastic precursor front, but it gives also a higher propagation velocity for the second (plastic) wave. Introducing the

nonlinear viscosity, which was described by the Swegle-Grady relationship [31] $\dot{\gamma}_p = A'(\tau - Y/2)^2$, we have received the profile "c" that reproduces reasonably well the plastic wave rise time and its propagation velocity. However, in all these three cases we have got a large amplitude of the elastic unloading wave which does not agree with the experimental data: while the unloading front arrives to the sample surface at the same time moment in calculated and measured free surface velocity profiles, the experimental velocity history shows slower unloading than calculated profiles. We may consider this discrepancy as an evidence of some softening of the material. Simulation for the elastic-isotropic body, for which the yield stress drops to zero when the elastic limit is reached, gives a much slower unloading wave but also the much slower plastic shock wave. The experimental velocity profile at unloading is situated between the free-surface velocity histories for elastic-plastic and elastic-isotropic bodies. It seems the softening of material as a result of high-rate deformation in the plastic shock wave leads to partial transition to the elastic-isotropic response.

Thus, comparison of the experimental data with the results of simulations with different simple models leads to conclusion that we have to account both the strain hardening and strain softening and to include the strain rate effect into the constitutive model. Our description of the elastic-plastic properties is based on the structural Marzing model which presents each elementary volume as a series of parallel elastic-viscous-plastic subelements [32] as it is shown in Figure 23 a,b. Subelements have equal elastic modules but different yield strength, Y_k , and viscosity. The deviatoric stress in elementary volume is determined as

$$\sigma = \sum_{k=1}^N \sigma_k g_k, \quad (6)$$

where N is amount of subelements, σ_k and g_k are the stress in subelement and the weight factor.

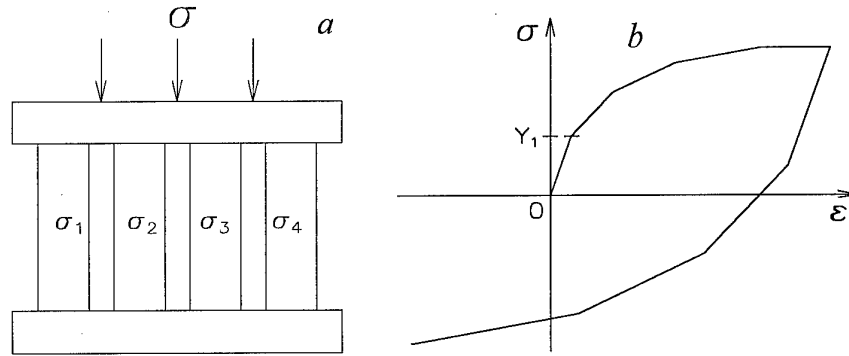


Figure 23. The structural multi-elements Marzing model (a) and its stress-strain diagram (b).

Our model consists of two elements ($N=2$), one of each is the strain hardening elastic-plastic body and the second is the elastic-viscous-plastic body with nonlinear viscosity described by the Swegle-Grady relationship:

$$\sigma_1 = Y_0 + Y' \epsilon_{1p}^n, \quad (7)$$

$$\dot{\epsilon}_{2p} = \frac{(\sigma_2 - Y_2)^2}{\eta_2} \quad \text{or} \quad \sigma_2 = Y_2 + \sqrt{\eta_2 \dot{\epsilon}_{2p}}, \quad (8)$$

where ε_{1p} and ε_{2p} are the plastic deformations in the elements.

The fraction of second component is growing as a result of inelastic deformation of the elementary volume as whole:

$$\dot{g}_2 = k_g(1 - g_2)\dot{\varepsilon}_p, \text{ where } \varepsilon_p = g_1 \cdot \varepsilon_{1p} + g_2 \cdot \varepsilon_{2p}; \quad g_1 = 1 - g_2. \quad (9)$$

Figures 24 to 26 present the results of computer simulations with the material parameters mentioned in the Table 5. A reasonably good agreement between the results of simulations and the experimental data and absence of steps and jumps in the pulse profile create a good base for simulations of the spall phenomena.

Table 5. Parameters of the constitutive elastic-viscous-plastic model for the materials tested.

Ingot	Y_0 , GPa	Y' , GPa	n	Y_2 , GPa	η_2 , Pa ² s ⁻¹	k_g
58784 (0.105%O ₂)	1.05	1.75	0.40	0.050	10 ¹¹	4
G3540 (0.198%O ₂)	1.00	2.25	0.35	0.075	10 ¹¹	4
64291 (0.24%O ₂)	0.80	2.50	0.30	0.130	5·10 ¹¹	4

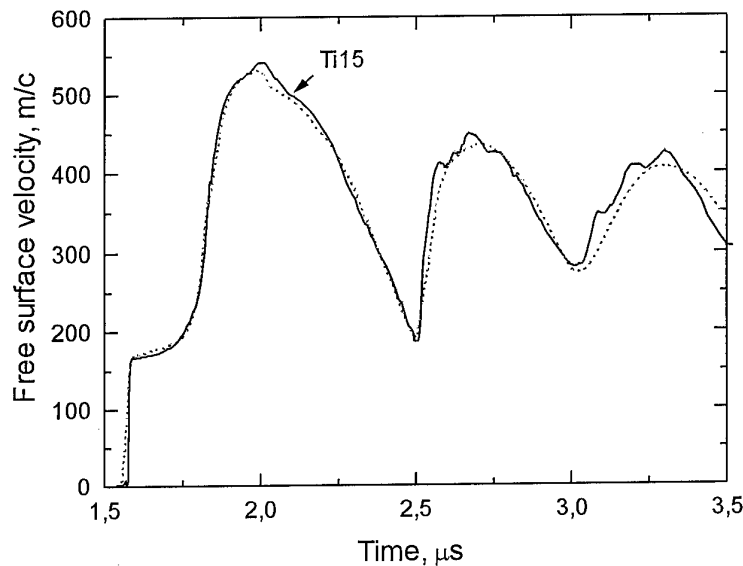


Figure 24. Result of computer simulation (dashed line) of the shot Ti15 with the ingot 58784 (0.105%O₂). The measured free surface velocity history is shown by the solid line.

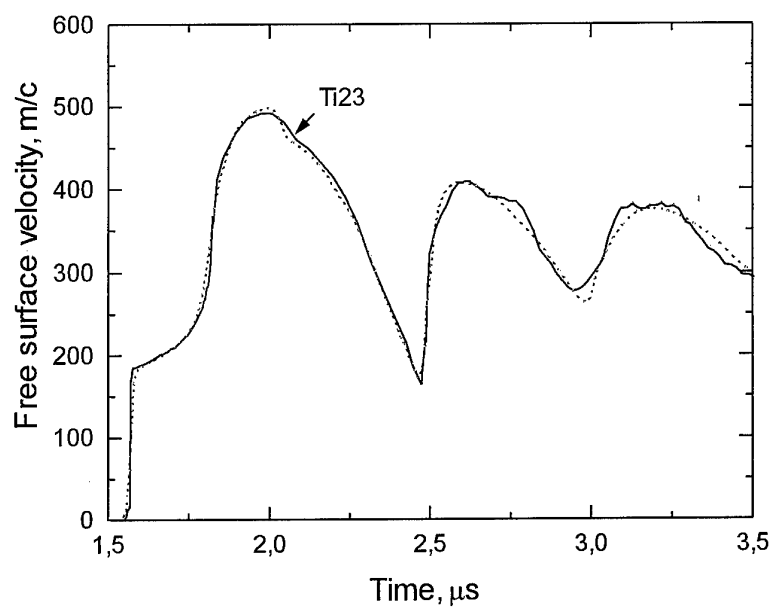


Figure 25. Result of computer simulation (dashed line) of the shot Ti23 with the ingot G3540 (0198%O₂). The measured free surface velocity history is shown by the solid line.

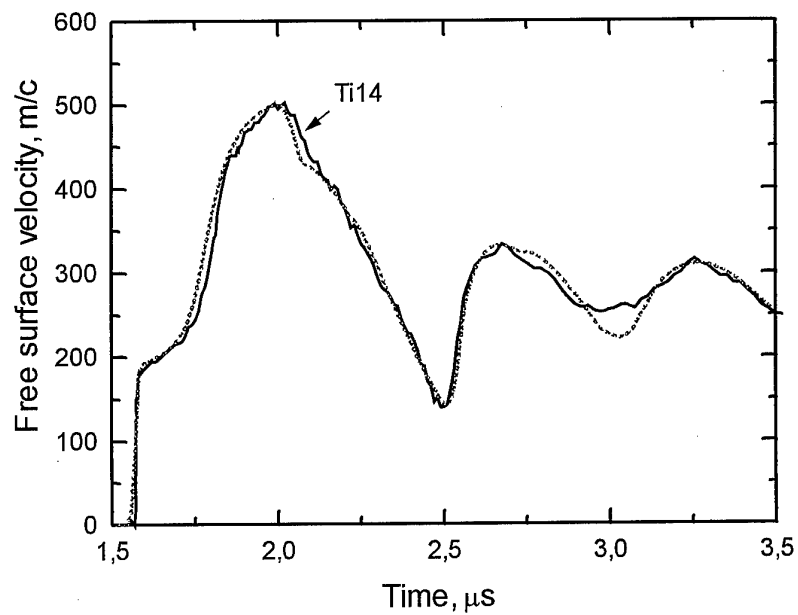


Figure 26. Result of computer simulation (dashed line) of the shot Ti14 with the ingot 64291 (0.24%O₂). The measured free surface velocity history is shown by the solid line.

The spall fracture was simulated using the model described in the ref. [33]. The damage was described by the specific volume of voids, V_v . The total volume V was presented as the sum of V_v and the specific volume, V_s , of undamaged (solid) material which is a function of pressure:

$$V = V_s(p) + V_v \quad (10)$$

The experimental data for the spall strength σ^* can be described by a power function of the expansion rate at unloading in the incident shock pulses:

$$\sigma^* = \sigma_n \cdot \left(\frac{\dot{V}}{\dot{V}_0} \right)^m \quad (11)$$

This empirical relationship reflects the damage-rate dependence on the applied tensile stress. Appearance of the spall signal means that the damage rate is four times the decompression rate in the incident load pulse, so we may interpret the empirical relationship (11) as:

$$\dot{V}_v = 4\dot{V}_0 (\sigma / \sigma_n)^\alpha, \quad (12)$$

where $\alpha = 1/m$.

The experimental profiles obtained do not indicate any notable delay of the fracture. Also, free-surface velocity profiles, as a rule, do not show notable stress relaxation ahead of the spall signal. This means that the obtained relation (12) describes the initial, or nearly initial, damage rate. Experimental profiles also show that the steepness of the spall pulse front is always proportional to the velocity gradient in the incident unloading wave. In other words, a faster initial damage rate is accompanied by a proportionally faster damage rate in the following phases of the fracture process.

It is clear that the damage rate approximately equals to the product of concentration of the damage nucleation sites times their average growth rate. Each material contains a spectrum of potential damage nucleation sites. Relatively coarse defects can be activated by low tensile stresses, while finer defects need higher stresses to activate them. According to known models, the growth of a void can be approximately represented as the product of a power function of its volume with the exponent less than 1, and a linear function of the tensile stress or pressure. Consistent with these guides to the fracture mechanisms, we were looking for a constitutive relationship in the simplest form

$$\frac{\dot{V}_v}{V_0} = \frac{\sigma}{\tau \sigma_n} \left(\frac{\sigma_{\max}}{\sigma_n} \right)^{\alpha-1} \left(\frac{V_v + V_{v0}}{V_0} \right)^\beta, \quad (13)$$

where σ_{\max} is the peak tensile stress which activates the damage nucleation sites at this point, constants σ_n and α are taken from the empirical relationship (12), the time factor τ , and the exponent β , as well as the initial volume of the damage nucleation sites, V_{v0} , are free parameters and have to be fitted.

Fracture was calculated using the empirical constitutive relationship (13) with parameters listed in Table 6. Figures 24 to 26 present results of calculations in comparison with experimental free-surface velocity profiles. Taking into account some natural uncertainty in the experimental conditions, we may conclude that this simplest empirical constitutive relationship (13) provides quite reasonable description of the spall process.

Table 6. Parameters of the fracture model.

Ingots	α	σ_n , GPa	β	V_{v0}/V_0	τ , ns
58784 (0.105%O ₂)	50	4.4	0.75	10 ⁻⁵	4.5
G3540 (0.198%O ₂)	50	4.4	0.75	10 ⁻⁵	2.3
64291 (0.24%O ₂)	50	4.4	0.70	10 ⁻⁵	114

DISCUSSION AND CONCLUSION

Table 7 summarizes the experimental data in comparison with quasistatic mechanical properties of the materials tested. The quasistatic mechanical properties are related to the loading in transversal direction since our in tests the loading was perpendicular to the rolling direction also. The dynamic yield strength and the spall strength in the table are average values over all experiments.

The table shows that the dynamic yield strength correlates well with the quasistatic yield strength. The quasistatic ultimate tensile strength is an integrated parameter which is determined not only by the true tensile strength but also by the strain hardening which controls a formation of neck in a sample at tension. Unlike quasistatic ultimate tensile strength, the shock-wave tests did not indicate a notable difference in the spall strength values of the three ingots tested. The specific energy of spall element separation, E_b , should be compared with the ductility which is characterized by elongation and reduction in area. Within an experimental uncertainty, which is estimated as $\pm 10\%$, the specific energy of spall element separation is practically the same for the all three ingots tested. It is close also to the value of $E_b = 1.3 \cdot 10^6$ J/m² determined earlier [18] for Ti-5Al-2.5Sn alloy although the critical diameter of spall element for this alloy was less than that for three materials tested in this work. However, basing on the whole sum of experimental data we may conclude that the material of the 64291 ingot is a best for armor purposes, because. While the dynamic yield strength, the spall strength, and the energy of spall element separation for this material are close for that of G3540, the 64291 ingot material with the largest oxygen content exhibits a greatest viscosity which leads to a faster decay of shock pulses.

The specific energy of spall element separation should characterize the energy loss for a fragmentation and determine the residual kinetic energy of the fragments. To verify an informativity of this parameter it would be useful to perform similar measurements for a wider set of materials, including steels. The wider data base will permit to look for a possible correlation between the energetic parameters of dynamic fracture and the fragmentation properties.

Table 7. Summary of quasistatic and dynamic mechanical properties.

Ingot	Ultimate Tensile Strength (GPa)	0.2% Yield Strength (GPa)	Elong. (%)	Reduct. in area (%)	HEL (GPa)	Dyn. Yield Strength (GPa)	Aver. Spall Strength (GPa)	E_f-E_{sp} (10^5 J/m ²)	E_b (10^6 J/m ²)
58784	0.93	0.84	12	30.5	2.2 ± 0.1	1.12	4.4 ± 0.2	1.4	1.5
G3540	1.03	0.96	15	31	2.5 ± 0.1	1.27	4.3 ± 0.2	1.3	1.3
64291	1.05	0.95	13	23	2.6 ± 0.1	1.32	4.4 ± 0.2	2.1	1.5

The computer simulations with the suggested models of inelastic shock deformation have shown a good agreement with the experimental free-surface velocity profiles that can be considered as an confirmation of the hypothesis about the temporal shock softening of the material. From this viewpoint it would be important to find a strain rate threshold above which the softening appears and to analyze its possible mechanisms and consequences. Probably we should reconsider results of rod impact tests accounting for the possibility of shock softening of materials. Another important aspect of the resistance to large dynamic deformation is a shear banding which is explained by local softening of the material as a result of its heating in the process of inelastic adiabatic deforming. To estimate possible contributions of these two mechanisms of softening the shock-wave experiments at elevated temperatures could be performed. Such experiments should provide both the initial yield stress and following resistance to dynamic strain which will be a valid base for analysis of mechanisms of the shear band instability.

The simulations have shown a good quality of description of the resistance to spall fracture. Since a constitutive relationship describing the dynamic fracture is necessary for any simulations of impact phenomena, it would be useful to find the model parameters for a wide set of materials. Coupled with determination of the statistical characteristics of potential damage nucleation sites in the matter the model should provide a complete description of the fracture properties.

It would be interesting to apply the models to a shock-wave response of hard brittle materials. In this sense, a comparative study of alumina ceramics and sapphire would be effective. Other potential object are a tungsten carbide and gradient materials based on ceramics and metals.

REFERENCES

1. U.Zwicker. *Titan und Titanlegierungen*. Springer-Verlag, 1974.
2. I.C.Jamieson, *Science*, **140**, 72 (1963).
3. B.Olinger, and J.C.Jamieson, *High Temp. - High Pressures*, **5**, 123 (1973).
4. V.A.Zilbershtein, N.P.Christotina, et al., *Fiz. Metal Metalloved. (USSR)*, **39**, 445 (1975).
5. A.R. Kutsar, V.N.German, and G.I.Nasova, *Acad. of Sciences USSR - Doklady (USSR)*, **213**, 81 (1973).
6. S.K.Sikka, Y.K.Vohra, and R. Chidambaram, *Prog. Mater. Sci.*, **27**, 245 (1982).
7. A.R. Kutsar, M.N. Pavlovsky, and V.V. Komissarov. *Letters to ZETF*, **35**(3), 91 (1982).
8. A.N. Kiselev, and A.A. Falkov, *Fiz. Goreniya i Vzryva (USSR)*, **18**, 105 (1982).
9. G.T. Gray III, *Shock Compression of Condensed Matter - 1989*, ed.: S.C. Schmidt, J.N.Johnson, and L.W.Davison Els. Sc. Publ. B.V., 407 (1990).
10. W. Gooch, M.S.Burkins, H.-J. Ernst, and T.Wolf. Ballistic performance of titanium against laboratory penetrators with aspect ratios of 10 or greater. *Proceedings of 15th International Ballistic Symposium*, 1995.
11. W.Gooch, M.S.Burkins, H.-J. Ernst, and T.Wolf. Ballistic penetration of titanium alloy Ti-6Al-4V. *Proceedings of the Lightweight Armour Systems Symposium*, The Royal Military College of Science, Shrivenham, Swindon, England, 1995
12. W.Gooch, M.S.Burkins, and K. Frank. Ballistic performance of titanium against laboratory penetrators. *Proceedings of 1st Australian Congress on Applied Mechanics '96*, Melbourne, Australia, 1996.
13. Novikov S.A., Divnov I.I., Ivanov A.G. (1966). The Study of Fracture of Steel, Aluminum, and Copper under Explosive Loading. - *Phys. of Metals and Metal science (USSR)*, **21**(4) pp.608-615.
14. Kanel G.I. and Petrova E.N. The Strength of Titanium BT6 at Shock-Wave Loading. In: "II Workshop on Detonation" (USSR), Chernogolovka, 1981, pp.136-142.
15. Ivanov A.G. Spallation in the Quasiacoustic Approach. *Phys. Phys. of Combustion and Explosion (USSR)*, 1975, No.3, pp.475-480.
16. Kanel, G.I. (1982). The work of spall fracture. - *Phys. of Combustions and Explosions (USSR)*, No 4, pp.84-88.
17. Grady, D.E. (1988). The spall strength of condensed matter. - *J. Mech. Phys. Solids*, **36**, No 3, pp.353-384.
18. Razorenov S.V. and Kanel G.I. (1991). The study of edge effects under spallation. - *Problems of Strength (USSR)*, No 9, pp.52-55.
19. S.V. Razorenov, A.V. Utkin, G.I.Kanel, V.E. Fortov, A.S. Yarunichev, K. Baumung, and H.U. Karow. Response of high-purity titanium to high-pressure impulsive loading. *High Pressure Research*, **13**, pp. 367-376 (1995).
20. Kanel, G.I., S.V. Razorenov and V.E Fortov (1987). The spall strength of metals in a wide range of shock load amplitudes. - *Acad. of Sciences USSR - Doklady*, v.**294**, No 2, pp. 350-352.
21. Me-Bar, Y., M. Boas and Z. Rosenberg (1987). *Mat. Sci. Eng.* **85**, p.77.
22. C.E. Morris, M.A. Winkler, and A.C. Mitchell. Ti-6%Al-4%V alloy wave profile measurements in the shadow region. In: *Shock Waves in Condensed Matter 1987*, eds: S.C. Schmidt and N.C. Holmes, Elsevier Science Publishers B.V., 1988, pp. 265-268.
23. L.C. Chhabildas, L.M. Barker, J.R. Asay, and T.G. Trucano. Spall strength measurements on shock-loaded refractory metals. In: *Shock Waves in Condensed Matter 1989*, eds: S.C. Schmidt et al., Elsevier Science Publishers B.V., 1990, pp. 429-432.

24. P. Andriot, P. Lalle, and J.P. Dejean. Quasi-elastic behavior of pure titanium and TA6V4 titanium alloy at high pressure. In: *High-Pressure Science and Technology - 1993*. Eds.: S.C.Schidt et al., AIP Conference Proceedings 309, pp.1009-1012 (1994).
25. G.I.Kanel, S.V.Razorenov, V.E.Fortov. *J. Techn. Phys. (USSR)*, **56**(3), 586 (1986)
26. K.E. Froeshner, D.E. Maiden, and H.H. Chau. Spall due to short high-intensity impulses. *J. Appl. Phys.* **65**(8), 2964-2973 (1989)
27. V.K. Golubev, S.A. Novikov, Yu.S. Sobolev, and N.A. Yukina. On character of the spall fracture of molybdenum, nickel, and titanium. *Problems of strength (USSR)*, 1985, No. 4, pp.64-66.
28. Barker L.M. and R.E.Hollenbach. *J. Appl. Phys.*, 1972, **43**, p. 4669.
29. Asay, J.R. and L.M. Barker (1974). Interferometric measurement of shock-induced internal particle velocity and spatial variations of particle velocity. - *J. Appl. Phys.*, 1974, **45**, No 6, pp. 2540-254
30. A.V.Bushman, G.I.Kanel, A.L.Ni, V.E.Fortov. *Intense Dynamic Loading of Condensed Matter*. Taylor & Francis, 1993, 287 pp.
31. Swegle, J.W. and Grady, D.E. *J. Appl. Phys.*, **58**, p.692 (1985).
32. Gokhfeld, D.A. and Sadakov, O.S. *Plasticity of Structural elements under Repeated Loads*. (in Russian). Mashinostroenie, Moscow, 1984.
33. G.I. Kanel, S.V. Razorenov, A. Bogach, A.V. Utkin, and D.E. Grady. Simulation of Spall Fracture of Aluminum and Magnesium Over a Wide Range of the Load Duration and Temperature. *International Journal of Impact Engineering*, **19**, pp. 467-478 (1997).